ROYAL SOCIETY OF CHEMISTRY

PAPER

Check for updates

Preclinical assessment of pan-influenza A virus CRISPR RNA therapeutics in a human lung alveolus chip

Yuncheng Man, [ab] Ryan R. Posey,[a] Haiqing Bai,[a] Amanda Jiang,[ab] Pere Dosta, [acd] Diana Ocampo-Alvarado,[ac] Roberto Plebani,[ae] Jie Ji,[a] Chaitra Belgur, [a] Natalie Artzi[acd] and Donald E. Ingber [*abf]

CRISPR technology offers an entirely new approach to therapeutic development because it can target specific nucleotide sequences with high specificity, however, preclinical animal models are not useful for evaluation of their efficacy and potential off-target effects because of high gene sequence variations between animals and humans. Here, we explored the potential of using the CRISPR effector Cas13 to develop a new therapeutic approach for influenza A virus (IAV) infections based on its ability to specifically and robustly cleave single-strand viral RNA using a complementary CRISPR RNA (crRNA). We engineered crRNAs to target highly conserved regions in the IAV genome to create a potential pan-viral treatment strategy. A human lung alveolus chip (Lung Chip) lined by human primary alveolar epithelial cells interfaced with human primary pulmonary microvascular endothelial cells and infected with a pandemic IAV H3N2 strain was used to evaluate the on-target and off-target effects of these antiviral crRNA therapeutics. Our data show that the crRNAs targeting highly conserved regions in the IAV genome potently reduced viral replication in the alveolar airspace in the Lung Chip, and this was accompanied by suppression of the human host inflammatory response as indicated by a significant reduction in cytokine production and recruitment of immune cells. Importantly, only minimal off-target effects were observed based on transcriptomic analyses. As these crRNAs inhibit replication of influenza H1N1 and H3N2 in A549 cells as well as H3N2 in Lung Chips, these findings support use of CRISPR-Cas13 as a potentially viable approach to develop pan-IAV therapeutics for combating future influenza pandemics. The results also demonstrate that human Organ Chips be useful as more clinically relevant preclinical models for testing the efficacy and safety of crRNA therapeutics.

Introduction

The discovery of the clustered regularly interspaced short palindromic repeats (CRISPR)-Cas gene editing mechanism in bacteria that can target specific gene sequences, and its application to enable gene editing in human cells, has led to

[a] *Wyss Institute for Biologically Inspired Engineering, Harvard University, Boston, MA 02215, USA. E-mail: don.ingber@wyss.harvard.edu*

[b] *Vascular Biology Program, Boston Children's Hospital and Harvard Medical School, Boston, MA 02115, USA*

[c] *Department of Medicine, Division of Engineering in Medicine, Brigham and Women's Hospital, Harvard Medical School, Boston, MA 02115, USA*

[d] *Institute for Medical Engineering and Science (IMES), Massachusetts Institute of Technology, Cambridge, MA 02139, USA*

[e] *Center for Advanced Studies and Technology (CAST), Department of Medical, Oral and Biotechnological Sciences, 'G. d'Annunzio' University of Chieti-Pescara, Chieti, Italy*

[f] *Harvard John A. Paulson School of Engineering and Applied Sciences, Harvard University, Boston, MA 02134, USA*

explosive development of myriad new analytic and therapeutic approaches. In particular, CRISPR-Cas13 has been used to repress eukaryotic gene expression at the posttranscriptional level where mRNA is modified by the class II, type VI CRISPR-associated RNA-guided ribonuclease.[1] The RNA-guided RNase Cas13 combines with a 64–66 nt CRISPR RNA (crRNA) containing a customizable sequence (22–30 nt spacer) that binds to a complementary sequence within the target RNA.[2,3] Upon binding, Cas13 cleaves the RNA at the binding site, and knocks down expression of the desired cellular RNA targets.[4] This approach can result in rapid (<24 h) and highly efficient posttranscriptional suppression of gene expression, including in mammalian cells.[5,6]

Here, we developed potential crRNA therapeutics directed against influenza A virus (IAV) infections because they have been the cause of six major flu pandemics responsible for 50–100 million deaths globally.[7–9] According to the U.S. Centers for Disease Control and Prevention, influenza still causes 9–41 million illnesses, 140 000–710 000

hospitalizations and 12 000–52 000 deaths annually in the U.S. alone.[10] Drug and antibody treatments for influenza infection have been developed, but they often trigger virus mutations, resulting in therapeutic resistance or escape.[11,12] Influenza vaccine development is also challenged by antigenic shift, drift, and reassortment.[13] As a result, IAV infections remain a major public health concern with the potential to generate future pandemics. To confront this challenge, in 2019, the CRISPR-Cas13 system was introduced as a programmable antiviral platform against IAV.[14] Later, a prophylactic CRISPR-Cas13-based antiviral approach was shown to strongly inhibit IAV infection (>50%) in vitro in a human lung epithelial cell line as well as in chicken cells.[15,16] More recently, an inhalable, mRNA-encoded CRISPR-Cas13 therapy against influenza infection was demonstrated in mice and hamsters, where IAV inhibition in animal lung tissues was consistent and highly potent against several H1N1 and H3N2 strains and across multiplicities of infection (MOIs).[17,18] Open sources for optimized guide RNA design to target viral RNA genomes have also been developed.[19,20]

The aforementioned studies have demonstrated the potential value of antiviral crRNA therapeutics against influenza infections; however, significant challenges remain. First, crRNA and gene target interactions are so specific and sensitive that the efficacy of antiviral crRNA therapeutics targeting human IAVs or human gene sequences cannot be assessed in animal models. These human-specific therapeutics need to be assessed in human primary cells, preferably when growing within a three-dimensional (3D) tissue- and organ-relevant context and exposed to relevant physical and chemical cues, rather than in established cell lines or even human primary cells in static 2D cultures. This is particularly important for human lung that is exposed to air while experiencing dynamic breathing motions. Second, off-target effects and potential toxicities of crRNAs cannot be analyzed in animal models because humans and animals share different genomes, anatomy, immune systems, and physiology.

Recent development of human Organ-on-a-Chip (Organ Chip) microfluidic culture technology that replicates human organ-level physiology and disease states,[21,22] including IAV infection,[23–25] with high fidelity offers a potential way to overcome these limitations. Here, we leveraged a previously described human lung alveolus chip (Lung Chip) model of IAV infection.[24] The Lung Chip was chosen over standard organoids or other in vitro lung models because these models do not replicate tissue–tissue interfaces, vascular perfusion, circulating immune cells, or organ-specific mechanical cues that are critical for accurate modeling of host cells that reside in a complex, dynamic lung microenvironment and their responses to influenza viral infection and CRISPR antiviral treatment. Here, we used the Lung Chip to assess the on- and off-target effects of crRNAs that were designed to target highly conserved regions within the IAV genome. These studies confirmed that the human Lung Chip can be used to validate the antiviral efficacy of these novel crRNAs as well as

analyze their off-target effects in vitro. These findings demonstrate the possibility of developing pan-IAV CRISPR RNA therapies for existing and emerging variants, and show that human Organ Chips may provide a valuable preclinical testbed for this new class of therapeutics.

Results

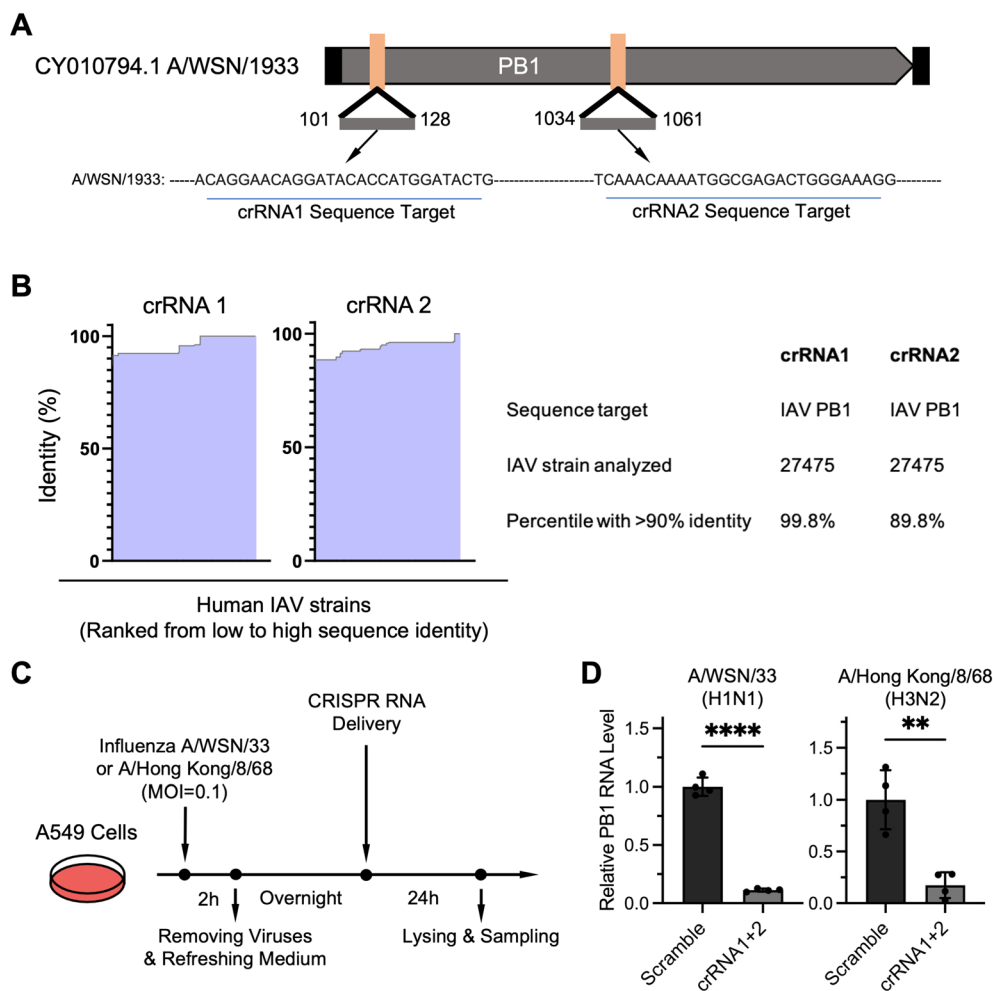### Pan-IAV crRNA sequence analysis and testing in A549 cell cultures

Two crRNAs (crRNA1 and 2) were designed and employed in this study that target conserved regions in influenza polymerase basic 1 (PB1) (Fig. 1A). We compared the crRNA sequences across all available IAV variants in the National Center for Biotechnology Information (NCBI) influenza virus database (with type A and human host), where we found that crRNA1 and 2 have >90% identity over 99.8% and 89.8% of the viral PB1 sequences, respectively, suggesting strong pan-IAV potential (Fig. 1B). We first tested the antiviral effect of the crRNAs in static 2D cultures of A549 human lung epithelial cell line infected with influenza A/WSN/33 (H1N1) or A/Hong Kong/8/68 (H3N2) for 2 h at a MOI of 0.1 (by estimating 240 000 cells at confluency in each well of a 24-well plate) (Fig. 1C). The supernatants with viruses were then removed and the A549 cells were incubated at 37 °C overnight before Cas13d mRNA (1 pmol) and a combination of crRNA1 and 2 (100 pmol each) were delivered into each well using Lipofectamine MessengerMAX (LMM). The cells were lysed for RNA extraction 24 h later and viral RNA levels were evaluated using reverse transcription-quantitative polymerase chain reaction (RT-qPCR). Control groups were treated with Cas13d mRNA (1 pmol) and scrambled guides (200 pmol).

These studies revealed that the crRNAs produced a strong knockdown effect, reducing viral PB1 RNA levels in the A549 cells by >80% for both IAV strains, compared to the scrambled controls (Fig. 1D). The study using the A549 cell line under static culture conditions demonstrated the antiviral potential of the crRNAs; however, we next sought to explore their efficacy and safety in the more physiologically relevant human Lung Chip model.

The human Lung Chip and infection with IAVs

The Lung Chip employed in this study has been previously described and fully characterized.[24] The model utilizes a commercially available microfluidic device containing two parallel channels separated by a porous membrane (Emulate Inc., Boston, MA). The membrane is coated with extracellular matrix (ECM) and human primary alveolar epithelial cells (AECs) are cultured under the air–liquid interface (ALI) on one side of the membrane in the apical channel, while human pulmonary microvascular endothelial cells (HPMECs) are cultured on the opposite side and exposed to dynamic fluid flow of culture medium through the basal channel (Fig. 2A). The physical effects of rhythmic breathing motions are simulated by applying cyclic suction to side chambers of

Fig. 1 Pan-IAV crRNA sequence analysis and 2D A549 cell line testing. (A) Schematic representation of influenza A/WSN/33 PB1 genome showing the conserved regions as targets for crRNA1 and 2. (B) Percent identity of the crRNAs with the analyzed human IAV variants in the NCBI influenza virus database. Colored region indicates the rank of the variants based on the identity compared with the crRNA sequence. (C) Overview of the experiment timeline of the 2D A549 cell line testing. (D) Treatment with the crRNAs significantly reduces the viral PB1 RNA level in A549 cells after influenza H1N1 or H3N2 infection compared to the scrambled control. N = 4 samples in each group with unpaired t-test.

the flexible device, which reversibly stretch and relax the flexible porous membrane and attached cell layers (Fig. 2A). Live cell imaging over time showed AECs and HPMECs seeded in the chip forming tissue monolayers that were closely apposed across the porous membrane (Fig. S1A). The barrier integrity of the established alveolar-capillary interface was also evidenced by confocal imaging of epithelial and endothelial cell–cell junctions and observing a significant decrease in barrier permeability which Lung Chips were compared to empty chips on day 11 (Fig. S1B and C). Notably, we observed significantly enhanced epithelial cell–cell junction expression in chips on day 11 compared to those on day 5 (Fig. S1B), consistent with maturation of the alveolar tissue barrier. In addition, we have previously demonstrated that the AECs within these chips can be infected by introducing influenza A/Hong Kong/8/68 (H3N2) virus (MOI = 1 by estimating 50 000 epithelial cells per chip) into the apical channel and that this infection is mediated by expression of α-2,3-linked sialic acid receptors on the surface

of these cells.[24] Here, we used the same Lung Chip influenza infection model and confirmed that the AECs were successfully infected with H3N2 using immunofluorescence microscopy, which revealed high levels of influenza viral NP expression (Fig. 2B) as observed in past studies using this model.[20] Moreover, when we collected apical washes from chips infected with virus and analyzed viral titers in plaque assays, we observed significant increases in viral load over time, which peaked at 48 h after chip infection and remained equally high level at 72 h (Fig. 2C).

Optimization of RNA delivery

To study the effects of crRNAs on IAV infection, we first compared transfection efficiencies of multiple RNA delivery vehicles. We analyzed LMM, a liposome-based RNA delivery platform that has been previously used to deliver Cas13d mRNA for treatment of coronavirus infection,[26] as well as two lipid nanoparticle (LNP) formulations based on 4-(dimethylamino)-
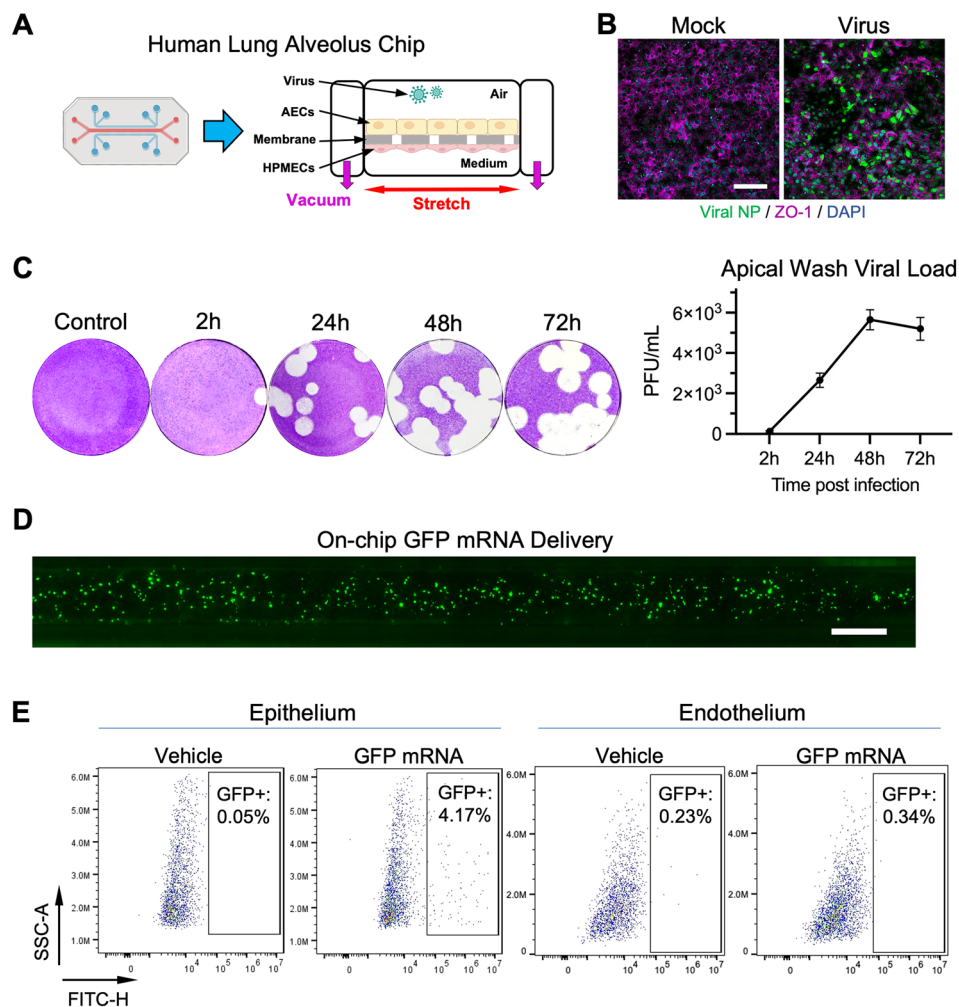
Fig. 2 Human Lung Chip for preclinical assessment of pan-IAV crRNAs. (A) Schematics of the human Lung Chip with the ECM-membrane lined with human primary alveolar epithelial cells (AECs) and human primary pulmonary microvascular endothelial cells (HPMECs). AECs were cultured in air and HPMECs were exposed to dynamic fluid flow of culture medium in the basal channel. The physical effects of rhythmic breathing motions are simulated by applying cyclic suction to side chambers which reversible stretch and relax the porous membrane and attached cell layers. (B) Fluorescent microscopic images of mock infected or H3N2 infected epithelium on chip showing influenza viral (nucleoprotein) NP, ZO-1 junctions, and nuclei. (C) Viral titers in the apical wash samples of infected chips at 2 h, 24 h, 48 h and 72 h post infection timepoints analyzed by plaque assays. N = 2 chips were continuously monitored and analyzed. (D) Fluorescent image showing the whole channel following transfection with GFP mRNA. Scale bar indicates 1 mm. (E) Flow cytometry analysis of GFP positive epithelial cells and endothelial cells showing on-chip transfection efficiency.

butanoic acid, (10Z,13Z)-1-(9Z,12Z)-9,12-octadecadien-1-yl-10,13-nonadecadien-1-yl ester (MC3) or 3,6-bis[4-[bis(2-hydroxydodecyl)amino]butyl]-2,5-piperazinedione (CKK-E12).[27,28] A single-channel microfluidic mixer for mixing the lipid phase and the aqueous phase of the solutions necessary for successful generation of LNPs was reproduced based on a previous published study (Fig. S2A and B).[29] We also studied a panel of polymeric nanoparticles based on poly(beta-amino esters) (pBAE NPs) (Fig. S2C, S3A and B) that were selected because they have been reported to successfully deliver mRNA or small guide RNAs *in vitro* or *in vivo*.[30–32] To perform higher throughput screening, we used Transwell cultures of human primary AECs cultured under an ALI to mimic the chip apical channel (albeit under static conditions), and similar studies were carried out using A549 cell cultures in parallel. To compare the delivery vehicles, green fluorescent protein (GFP)-encoding mRNA (0.6 or 1 μg)

was delivered into individual cultures, incubated overnight, and analyzed using either fluorescence microscopy or by flow cytometry after trypsinization.

Fluorescence microscopic imaging revealed that the RNA delivery platforms exhibit different transfection efficiencies in these two cell types, with lower efficiencies being observed in the more clinically relevant human primary AECs compared to the established A549 lung cell line (Fig. S4A and B). In the AECs, LMM resulted in the highest transfection efficiency, which was followed by the histidine-modified pBAE NPs (Fig. S4C). Thus, we selected LMM for on-chip mRNA delivery in all subsequent studies, which resulted in approximately 4% GFP-positive AECs compared to the vehicle control that was almost completely free of GFP staining (Fig. 2D and E). Notably, GFP-positive endothelial cells were negligible in the GFP
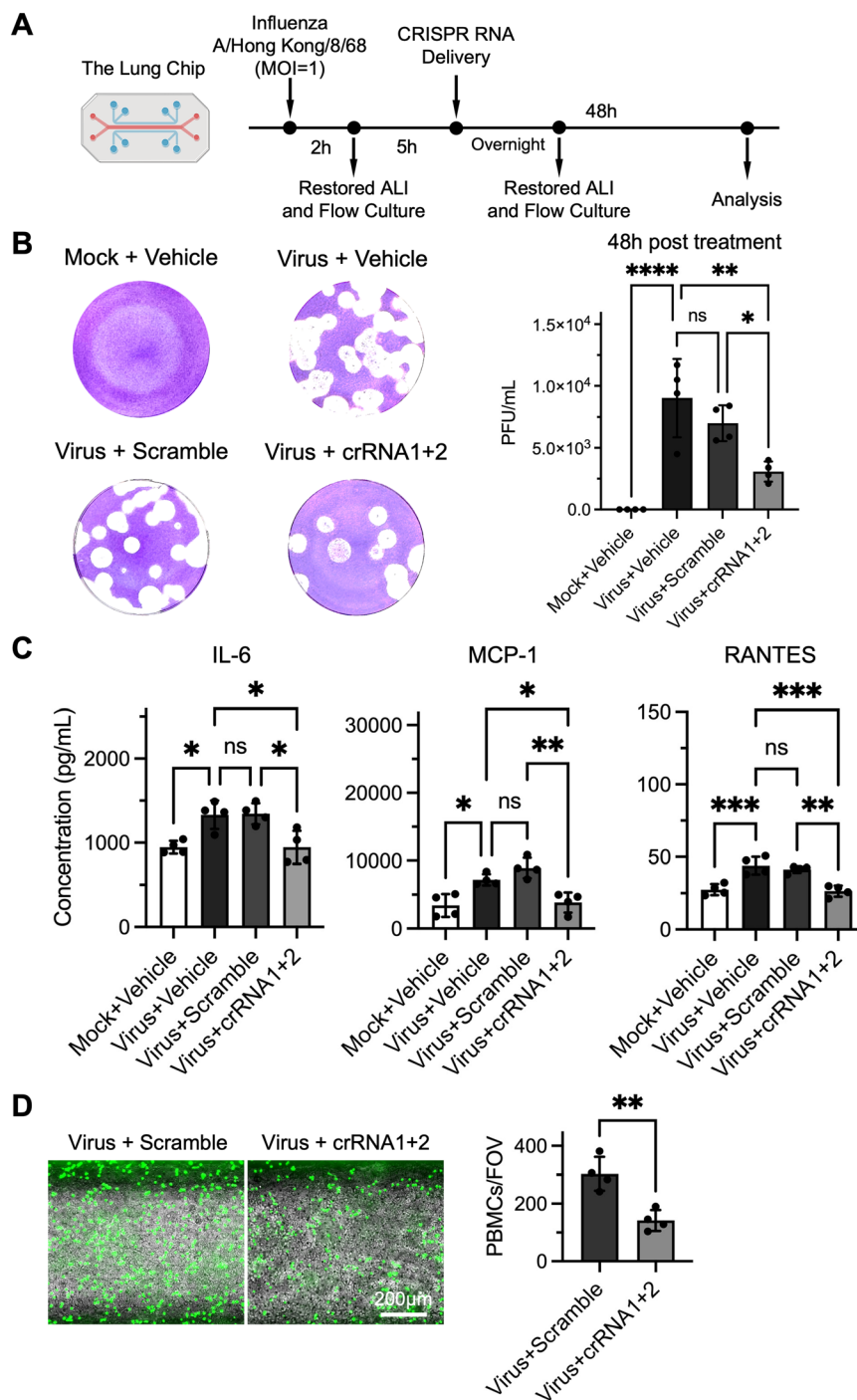
Fig. 3 Treatment with pan-IAV crRNAs after influenza infection reduces viral titers and vascular inflammation in the human Lung Chip. (A) The experimental timeline. Chips were infected with influenza A/Hong Kong/8/68 at MOI of 1 for 2 h statically, and transfected with Cas13d mRNA plus crRNAs or scrambled guides 5 h after infection. Apical wash was collected at the 48 h timepoint following treatment for viral titer analysis. Vascular effluents were collected the same time for cytokine production analysis. (B) Plaque assays show that influenza infection induced significant viral titers in the apical wash samples from infected chips compared to mock infected chips, and viral titers are significantly reduced in chips treated with the crRNAs compared to those treated with scrambled control at the 48 h timepoint following treatment. (C) Luminex analyses show that influenza infection induces significantly elevated vascular effluent levels of IL-6, MCP-1 and RANTES in infected chips compared to mock infected chips. In addition, these cytokine levels are significantly reduced in chips treated with the crRNAs compared to those treated with scrambled control at the 48 h timepoint following treatment. (D) Representative microscopic images showing vascular peripheral blood mononuclear cell (PBMC) recruitment. The number of recruited PBMCs to vascular endothelium are significantly reduced in chips treated with the crRNAs compared to those treated with scrambled control at the 48 h timepoint following treatment. $N = 4$ chips in each group. Each data point in (D) represents an averaged number of PBMCs across 6 different fields of view obtained from one chip.
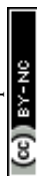
mRNA transfected group compared to the vehicle control group, indicating that crRNA delivery through the epithelial cell channel resulted in minimal endothelial cell transfection (Fig. 2E).

Pan-IAV crRNAs reduce viral infection and inflammation in the human Lung Chip

We next analyzed the on-target effect of the pan-IAV crRNAs in Lung Chips that were infected with influenza H3N2 or mock infected (incubated with blank culture medium) for 2 h under static conditions (Fig. S5A) before ALI and cyclic breathing motions were restored, and then RNA was delivered to the chips 5 h later (Fig. 3A). The 5-hour period was intended to allow for at least one cycle of IAV replication, as well as to simulate the time between symptom onset and treatment initiation in patients. Viral titers in apical wash samples were also analyzed at this timepoint before the crRNA treatment, demonstrating consistency among the infected chips (Fig. S5B). Thereafter, the H3N2 infected chips were transfected with vehicle, Cas13d mRNA (1 pmol mL^{-1}) plus scrambled guides (200 pmol mL^{-1}), or Cas13d mRNA plus the combination of crRNA1 and 2 (100 pmol mL^{-1} of each), while mock infected chips were transfected with vehicle alone, and the next morning an ALI was restored within the apical channels of all chips. This method simulates treatment through airway inhalation. When we analyzed apical wash samples at 48 h post treatment, we found significantly elevated viral titers in infected chips treated with vehicle, compared to mock infected chips using plaque assays (Fig. 3B). Importantly, at the same timepoint, there were significantly reduced viral titers in apical washes from infected chips treated with crRNA1 and 2 compared to infected chips treated with scrambled guides (Fig. 3B). No difference was observed in the viral titers between infected chips treated with vehicle and those with scrambled guides, confirming that the scrambled guides have no antiviral activity. These results indicate that the crRNAs strongly inhibit viral replication within the infected human primary AECs when cultured on-chip in an organ-relevant context, which ultimately leads to reduced virions in the alveolar airspace. Moreover, the strong antiviral effect of the crRNAs on both the H1N1 strain and the H3N2 strain in A549 cell cultures as well as the H3N2 strain in the Lung Chips demonstrate that these pan-IAV crRNAs can produce broad-spectrum viral inhibition.

To further evaluate the potential therapeutic impact of the crRNAs, we collected vascular effluents at 48 h post treatment and carried out inflammatory cytokine analysis. H3N2 infection of the Lung Chips resulted in increased inflammation as shown by significantly elevated levels of interleukin-6 (IL-6), monocyte chemoattractant protein-1 (MCP-1), and regulated on activation, normal T cell expressed and secreted (RANTES) protein in infected chips compared to mock infected chips (Fig. 3C). Importantly, at 48 h post treatment, we found significantly reduced cytokine levels in infected chips treated with crRNA1 and 2, compared to

infected chips treated with scrambled guides (Fig. 3C). In contrast, no difference was observed in the cytokine levels between infected chips that were transfected with vehicle and those transfected with scrambled guides (Fig. 3C). To further verify these findings, we introduced peripheral blood mononuclear cells (PBMCs) into the basal vascular channel and performed an immune cell recruitment assay. The average number of PBMCs recruited to the surface of the vascular endothelium detected per field of view (FOV) was significantly lower in infected chips treated with crRNA1 and 2, compared to infected chips treated with scrambled guides (Fig. 3D), which is consistent with the results of the cytokine analysis. Altogether, these results suggest that the pan-IAV crRNAs effectively reduce host inflammatory responses after IAV infection as well as inhibiting viral replication.

Transcriptomic analysis of potential off-target effects of pan-IAV crRNAs

Finally, we sought to detect potential off-target effects of the pan-viral crRNAs, which is a major concern for implementing CRISPR-Cas systems for human gene editing therapies that cannot be effectively assessed in animal models. RNA was extracted from epithelial cell lysates from the Lung Chips and bulk RNA-sequencing (RNA-seq) was carried out ($N = 4$ in each group). Differential gene expression analysis of epithelial cells in infected chips *versus* mock infected chips revealed 1432 differentially expressed genes (DEGs) (Fig. S6A). Kyoto Encyclopedia of Genes and Genomes (KEGG) pathway analysis revealed upregulation of cytokine–cytokine receptor interactions and chemokine signaling pathways after viral infection (Fig. S6B), which were accompanied by increased expression of several inflammatory markers, including CCL5 and IL6. We also observed upregulation of cytosolic DNA sensing and RIG I receptor signaling pathways after viral infection, potentially associated with cellular viral RNA sensing and clearance, as well as upregulation of a number of innate immunity genes, such as interferon-B1 (IFNB1), IFNL1, MX1, MX2, OAS1, OAS2, OAS3, ISG15, IFI6 and IFI27 (Fig. S6A). These data confirm that the human Lung Chip faithfully replicates host innate immune responses of lung alveoli to IAV infection as demonstrated in previous studies.[24,25,33]

To interrogate whether the Cas13d protein and guides induce non-specific immune or stress responses in the epithelial cells, we analyzed cells from infected chips treated with Cas13d mRNA and scrambled guides and compared them to those from infected chips treated with vehicle. Impressively, no DEGs were observed (Fig. S6C), which suggests that Cas13d itself and scrambled guides have no off-target effects on immune or stress responses, in agreement with our observations that these constructs did not alter viral titer or cytokine production.

Finally, we performed a deep interrogation of potential off-target effects by analyzing cells from infected chips treated with crRNAs and compared them to those from
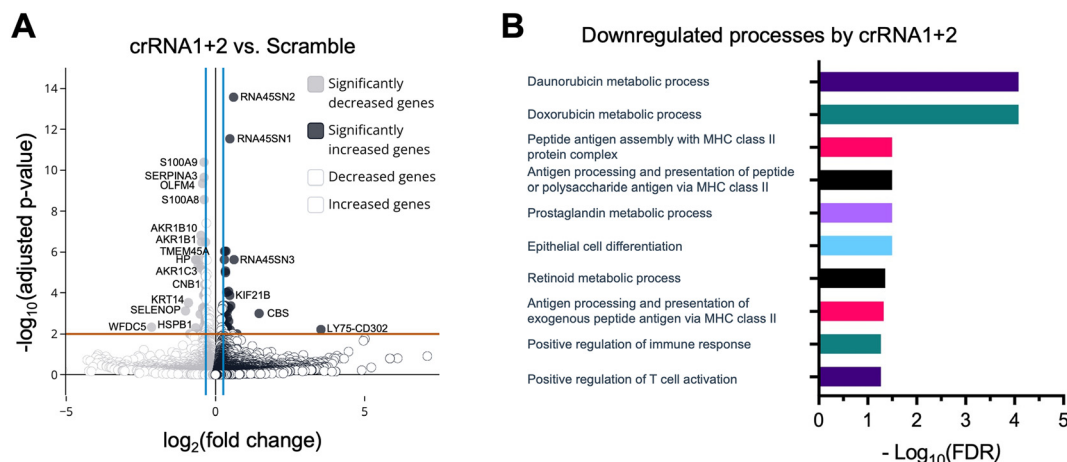
Fig. 4 Transcriptomic analyses of off-target effects of the pan-IAV crRNAs. (A) Volcano plot of DEGs comparing epithelial cells from infected chips treated with crRNA1 and 2 to those from infected chips treated with scrambled control. (B) Bar plot visualization of significantly downregulated processes (false discovery rate (FDR) <= 0.054) using the 38 downregulated DEGs identified following the crRNA treatment compared to the scrambled control. Analysis was performed using Database for Annotation, Visualization and Integrated Discovery (DAVID, **https://david.ncifcrf.gov/home.jsp**). N = 4 chips in each group.

infected chips treated with scrambled guides, which revealed 38 upregulated and 38 downregulated genes (Fig. 4A). KEGG pathway analysis of these results revealed downregulation of ribosome and intestinal immune network for IgA production pathways associated with the crRNA treatment. To determine whether the downregulated genes were mediated by direct Cas13d cleavage, we performed a Basic Local Alignment

Search Tool (BLAST) analysis on crRNA sequences against the "human genomic plus transcript" database and found a list of genes as top-scoring targets (Table 1). Notably, none of these top-scoring genes displays a 100% match with the crRNA sequences, and none of the significantly downregulated genes caused by the crRNA treatment was among the top-scoring targets. To gain more insight, we

Table 1 Sequences and top-scoring targets of the crRNA1 and crRNA2

crRNA1 sequence		crRNA2 sequence	
AACCCCUACCAACUGGUCGGGGU UUGAAAC ACAGGAACAGGAUACA CCAUGGAUACUG		AACCCCUACCAACUGGUCGGGGU UUGAAAC UCAAACAAAAUGGCGA GACUGGGAAAGG	
crRNA1 potential on-target genes		crRNA2 potential on-target genes	
Gene	Query cover (%)	Gene	Query cover (%)
CLRN3	46	ATP23	57
CMSS1	60	HOXA2	53
CPA4	46	CHD3	50
DDB1	46	MON1B	64
ELP5	46	WNK4	50
DNAJB1	60	CYTH3	50
LHX9	53	WT1-AS	50
POU6F2	60	CPLANE1	60
PRDM5	46	TDRD15	46
RNF111	60	EXT1	60
TMEM207	46	RTEL1	46
UBE2QL1	50	TMEM255B	53
WNT2	46	DENND1B	46
ZP2	50	PPOX	46
ZSWIM5	78	FLRT2	46
		SUPT6H	46
		PTPRZ1	46
		FAM184A	46
		WDFY4	46
		DYRK1A	46
		SLC25A35	46

Scrambled control sequence: AACCCCUACCAACUGGUCGGGGUUUGAAACUCACCAGAAGCGUACCAUACUCACGAAC.

performed gene set enrichment analysis (GSEA) using the 38 downregulated DEGs. We found significantly downregulated GO: biological process (GOBP), such as positive regulation of immune response and positive regulation of T cell activation (Fig. 4B). Taken together, these data suggest that the downregulated DEGs were not caused by off-target cleavage by Cas13d, but instead were due to reduced host inflammatory responses after the crRNA treatment. Altogether, our data strongly suggest that the targeted antiviral crRNAs we tested exhibit potent on-target antiviral effects and minimal off-target effects in the human Lung Chip preclinical model of IAV infection. These findings raise the possibility that this human Organ Chip model could be used for preclinical evaluation of the efficacy and safety of crRNA therapeutics before moving to the clinic in the future (Fig. 5).

Discussion

This study demonstrates for the first time that human Organ Chips may be used as a tool for preclinical assessment of CRISPR RNA therapeutics, and specifically for crRNAs targeting RNA viruses. We employed two crRNAs designed to target highly conserved regions in IAV genomic segment PB1, which represents a broad-spectrum antiviral strategy for current and potential future pandemic strains. Leveraging the human Lung Chip, we showed that the crRNAs effectively reduced viral titers in the alveolar airspace on-chip. These data confirm that the crRNA antivirals are functional when administered after infection and that they can suppress viral replication for at least 2 days once delivered into the cells. Importantly, to our knowledge, we demonstrated for the first time that this antiviral approach reduces host inflammatory responses, as evidenced by significantly reduced vascular cytokine levels and immune cell recruitment. Here, we only employed one simple combination of two crRNAs targeting the same viral gene and demonstrated its effectiveness.

However, the pan-IAV approach may provide even greater therapeutic value if multiple CRISPR guides engineered to target multiple conserved regions across all viral genome segments can be administrated at the same time. This approach warrants future investigation.

Despite the highly specific target knockdown activity of CRISPR-Cas13, a recent study identified significant off-target effects in cultured eukaryotic cells.[34] Considering that the catalytic site of Cas13d is located on the outside of the protein facing away from the crRNA–target RNA complex, collateral cleavages are not unexpected.[35] Here, to our best knowledge, we made the first attempt to analyze potential off-target effects of CRISPR-Cas13 antiviral approach in a human-relevant microphysiological system that emulates the complex multicellular composition, tissue–tissue interfaces, and dynamic physical and biochemical features of a major functional unit of a living organ – the lung alveolus. Notably, no DEGs were found when we treated cells with Cas13d mRNA and scrambled guides compared to those with vehicle only, suggesting that the Cas13d protein and guides do not induce immune or stress responses in cells. These findings also align with our viral titer and cytokine data, where delivery of Cas13d mRNA and scrambled guides had no effect. Moreover, our RNA-seq data revealed a number of significantly downregulated genes following the crRNA treatment, which were not caused by direct Cas13d cleavage due to little sequence identity between the genes and the crRNAs. Significant GOBP terms found using those downregulated genes revealed that they were associated with reduced host inflammation or downregulated antigen presentation processes, which is consistent with our observations of reduced viral titers and cytokine production following crRNA treatment. Altogether, these data suggest that the downregulated genes are related to the desired on-target effects of the crRNA antiviral therapeutic (*i.e.*, reduced viral
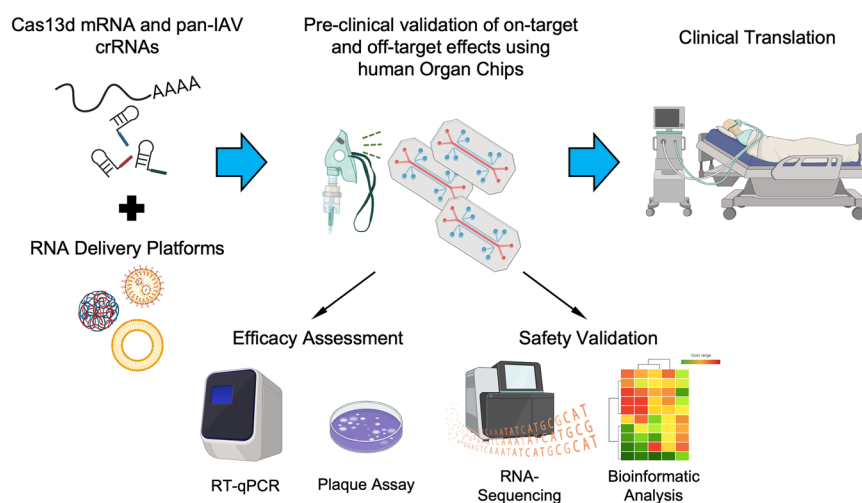

Fig. 5 Schematics of human Organ Chips as a useful preclinical tool for rapid efficacy assessment and safety validation of antiviral CRISPR RNA therapeutics for combating future influenza pandemics. Created with BioRender (**https://www.biorender.com/**).

infection and inflammation) and *not* to non-specific off-target effects.

It should be noted that we observed relatively modest mRNA delivery efficiency in human primary AECs on-chip, in agreement with the literature where highly differentiated respiratory epithelium are difficult to transfect.[36,37] Although several previous studies showed that MC3 and CKK-E12 LNPs enable RNA delivery in animals,[38–41] with some of them emphasizing delivery into the lung, we found that these two LNP formulations were unable to deliver mRNA into human AECs that were differentiated and cultured under in an ALI on-chip. We postulate that the conflicting results might be due to the discrepancy between animal and human physiology, which highlights the necessity of validating gene delivery platforms using human cells cultured in a physiologically relevant, organ-specific microenvironment. Despite the modest transfection efficiency, we still observed that the crRNA treatment reduced the viral replication and host inflammation, demonstrating the potency of the therapy. Other promising delivery platforms should be explored further as they could potentially enable allow more effective delivery of CRISPR-Cas13 constructs in the future. In addition, we found negligible transfection efficiency in endothelium and thus the off-target effect was primarily interrogated in epithelium. However, safety studies may also be carried out on endothelium in the future when developing CRISPR RNA therapeutics targeting host inflammatory genes that use different administration routes (*e.g.*, nebulization, intravenous injection). Furthermore, alterations in breathing motion pattern and vascular shear flow mediated by disease status may also have an impact on gene-based therapy delivery efficiency,[42–44] and the therapeutic efficacy may similarly depend on specific patient lung microenvironment (*e.g.*, presence of resident and/or circulating immune cells). Importantly, the Lung Chip provides a tool where contributions of individual factors, such as levels and frequencies of cyclic mechanical deformation, shear flow, and immune cells can be isolated and meaningfully analyzed, as demonstrated previously using Organ Chip models.[24,25,45,46]

As RNA viruses pose significant challenges for drug and vaccine development globally, the CRISPR-Cas13 antiviral approach could reshape the paradigm for therapeutic development. There are several widely recognized advantages of this approach. First, the mRNA delivered into cells can be rapidly translated into the desired protein which avoids safety issues such as genome integration or severe innate immune responses.[47–50] Second, while existing antiviral drugs and antibodies are clinically effective, drug resistance and impaired antibody binding efficiency of evolved viral variants have become a common problem.[51,52] In contrast, the crRNAs we developed are designed to target conserved regions in the viral genome and are therefore less susceptible of virus escaping mutations. Third, crRNAs can be easily and rapidly engineered for highly specific and rapid

suppression of viral gene expression, which has enormous potential therapeutic and commercial value.[53]

The past COVID-19 pandemic and potential future IAV pandemics pose a major threat to global health. The lack of a preclinical model that can faithfully recapitulate human physiology has greatly hindered the discovery and evaluation of novel therapeutics, which is also evidenced by the growing number of viral infection studies that using *in vitro* human lung alveolus models.[54–57] Human Organ Chips have been previously used to model spontaneous emergence of potential variants of concern through multiple chip-to-chip passages (mimicking human-to-human viral transmission).[58] Thus, this technology also may be useful for identifying crRNAs that can target new virus variants, and hence help to deliver effective therapies to patients before these variants spread widely through the population. Importantly, regulatory agencies are now encouraging pharmaceutical testing to use human Organ Chips and other human preclinical models,[59] and the U.S. Congress has passed the "FDA Modernization Act 2.0", which allows data obtained using alternative human-relevant *in vitro* models including human Organ Chips to be included in investigation new drug (IND) applications in place of date obtained through animal testing.[60] More recently, the U.S. Food and Drug Administration (FDA) announced their intent to phase out animal testing requirement for monoclonal antibodies and other drugs over the next 3–5 years, and the National Institutes of Health communicated that they will no longer fund research proposals that rely exclusively on animal testing. Thus, the use of human Organ Chips for novel therapeutic discovery is becoming more important than ever before.

Like all experimental investigations, this study has limitations that must be considered. First, the transfection efficiency using LMM was modest and required the inclusion of liquid in the airspace of the epithelial channel for several hours, which does not fully mimic local delivery in human lung alveoli. However, we have previously shown that therapeutics delivered *via* this route in human Lung Chips replicate effects observed when antiviral drugs are delivered intranasally *in vivo*.[23] Second, we carried out these studies with physiological breathing motions to mimic early stages of infection; however, viral infections can lead to cessation of mechanical deformations of alveoli due to accumulation of infection-associated inflammatory exudates, and we have shown that inhibition of breathing motions can further enhance viral replication and infection on-chip.[24] Inclusion of pulmonary macrophages also can influence the viral infection response in Lung Chips,[25] and thus, both of these features should be explored in future models of later stages of infection. We also recommend that future researchers carefully validate their human lung alveolus models by using various human primary AEC donors and commercial sources as the proportion of type I/II AECs can vary significantly depending on source, and over the course of extended cultures. Finally, it is important to note that while we targeted IAV infections here, the same approach can be

applied to develop and validate crRNA therapeutics preclinically for other viruses (*e.g.*, coronaviruses) and for any human-relevant RNA target.

Methods

crRNA design

crRNA1 and 2 were designed based on a previous study that utilized small interfering RNA (siRNA) to knock down the influenza viral genome.[61] The viral PB1 gene was selected because it functions as the catalytic core of the RNA-dependent RNA polymerase (RdRp) for viral RNA replication, thus highly conserved across IAVs due to its vital role.[62] The target sequences in the influenza PB1 gene were analyzed based on their conservation across various influenza subtypes and strains, including those from humans, chickens, ducks, horses, and swine, while ensuring no homology with any known human genes. To construct crRNA1 and crRNA2, a complementary spacer sequence (complementary to the target RNA) was linked to the 3′ end of the Cas13d direct repeat (DR).[6] All crRNAs were purchased from Integrated DNA Technologies (Coralville, IA). Cas13d mRNA was purchased from Creative Biogene, Inc. (Cambridge, MA). CleanCap® GFP mRNA was purchased from TriLink BioTechnologies (San Diego, CA). RNA concentrations were measured by absorbance at A260 using a NanoDrop. For RNA transfection efficiency analysis, following GFP mRNA delivery, cells in Transwell cultures or the Lung Chips were treated with TrypLE Express (Thermo Fisher Scientific, Waltham, MA) for 30 min at 37 °C, after which cells were collected in culture medium. Cells were washed twice with cold DPBS, and were re-suspended in Stain Buffer (BD Biosciences, San Jose, CA). The proportion of GFP positive cells were obtained by flow cytometry analysis.

Fabrication of LNPs and the microfluidic mixer

MC3 LNPs were prepared by combining an aqueous phase of diluted GFP mRNA in pH 3.0 citrate buffer (Alpha Teknova, Inc., Hollister, CA) and an organic phase of D-Lin-MC3-DMA (Echelon Biosciences, Inc., Salt Lake City, UT), DSPC (Avanti Polar Lipids, Inc., Alabaster, AL), cholesterol (Sigma Aldrich, St. Louis, MO), and DMG-PEG2000 (Avanti Polar Lipids) in ethanol at a molecular ratio of 50:10:38.5:1.5 and a MC3:mRNA mass ratio of 10:1 using a customized microfluidic mixer (as described below).[63] Similarly, CKK-E12 LNPs were prepared by combining an aqueous phase of diluted GFP mRNA in pH 3.0 citrate buffer and an organic phase of CKK-E12 (Echelon Biosciences), cholesterol, DOPE (Avanti Polar Lipids) and C14-PEG 2000 (Avanti Polar Lipids) in a molecular ratio of 35:46.5:16:2.5 and a cKK-E12:mRNA mass ratio of 10:1 using the microfluidic mixer.[27] For both LNP formulations, the aqueous phase and the organic phase were mixed at the volumetric ratio of 3:1 and the total flow rate in the microchannel was 200 μL min⁻¹.[28] For characterization, freshly prepared LNPs were characterized by dynamic light scattering (DLS) using Zetasizer Nano (Malvern PANalytical, Malvern, UK). Encapsulation efficiency was calculated by a Quant-iT RiboGreen assay (Thermo Fisher). Briefly, LNPs were either diluted in TE buffer as a control, or Triton X-100 to lyse the LNPs and were plated with RNA standards. The RiboGreen reagent was added, and fluorescence was measured by a plate reader. A standard curve was generated to quantify RNA content, and encapsulation efficiency (%) was calculated as follows: 100 × (total RNA − unencapsulated RNA)/(total RNA).

The microfluidic mixer used to fabricate nanoparticles utilizes a previously described single channel design.[29] Photomasks were purchased from Photronics, Inc. (Brookfield, CT). The microfluidic mixers were fabricated using standard soft lithography protocol.[64–66] Briefly, a layer of SU-8 2050 (Kayaku Advanced Materials, Westborough, MA) was initially spin-coated on top of a 3 inch silicon wafer (University Wafers, South Boston, MA) at 2100 rpm, which was followed by soft bake at 95 °C for 9 min. Thereafter, the wafer was UV-exposed for 30 s under the first photomask for microchannel geometry using a MA6 mask aligner. Post-exposure bake was performed at 95 °C for 7 min. Next, the wafer was developed in SU-8 developer for 6 min, rinsed by isopropanol, and air dried. A second SU-8 2010 (Kayaku Advanced Materials) layer was then spin-coated on top of the wafer at 1000 rpm for 30 s, which was followed by soft bake at 95 °C for 4 min. Thereafter, the wafer was aligned and UV-exposed for 20 s under the second photomask for staggered herringbone mixer structures on the MA6 mask aligner, which was followed by post-exposure bake at 95 °C for 4 min and development for 4 min. The wafer was finally hard baked at 110 °C overnight. The following day, the wafer was surface passivated using trichloro(1*H*,1*H*,2*H*,2*H*-perfluorooctyl) silane (Sigma Aldrich) under vacuum for 2 h to facilitate the separation of the molded polymer. Degassed polydimethylsiloxane (PDMS, Fisher Scientific, Hampton, NH) and curing reagent mixture (mass ratio 10:1) was poured on top of the wafer, which was cured in an oven at 65 °C overnight. The following day, the PDMS replicates were peeled from the wafer, cut into shape, cleaned with isopropanol, and irreversibly bonded to standard microscope glass slides by oxygen plasma treatment. The microfluidic mixers were rinsed with ethanol and DPBS before experiments and were disposed after single use.

Fabrication of pBAE NPs

Polypeptide-modified pBAE polymer was synthesized *via* a two-step procedure, as we described previously.[30–32] Briefly, pBAE polymerization was performed using 5-amino-1-penta-nol (0.426 g, 4.1 mmol), hexylamine (0.422 g, 4.1 mmol), and 1,4-butanediol diacrylate (2.0 g, 9.1 mmol) (Sigma Aldrich). pBAE polymerization was carried out under magnetic stirring at 90 °C for 24 h. pBAE apparent molecular weight was 2500 g mol⁻¹, confirmed by HPLC-SEC (relative to polystyrene standards) and proton nuclear magnetic resonance (hydrogen-1 NMR). Then, pBAE polymer was further modified with cationic polypeptide moieties (CPC Scientific, Sunnyvale,

CA) by adding the thiol group of cysteine-terminated polypeptides to the acrylate-terminated end-groups of pBAE polymer. The chemical structure of the resultant polymers was confirmed by the disappearance of acrylate signals and the presence of signals typically associated with polypeptides. For formulations, polyplexes were performed by mixing equal volumes of polypeptide-modified pBAEs and nucleic acids in acetate buffer at 12.5 mM and pH 5.5 (Sigma Aldrich). The polypeptide-modified pBAE was added to a solution of mRNA, mixed with pipetting for a few seconds and incubated at RT for 10 min. Then, the resulting nanoparticles were nanoprecipitate in DPBS. To assess mRNA retardation, different mRNA-to-polymer ratios (w/w) between 2:1 and 200:1 were studied. pBAE–mRNA complexes were freshly prepared and added to wells of agarose gel (2%, containing Sybr-safe, Thermo Fisher). Similarly, freshly prepared pBAE NPs were characterized by DLS.

Flow cytometry

Cell suspensions were analyzed by CytoFlex LX (Beckman Coulter, Brea, CA), and data were analyzed using FlowJo V10 software (FlowJo LLC, Ashland, OR).

RT-qPCR

RT-qPCR analysis was carried out by lysing A549 cells using Buffer RLT Plus (Qiagen, Hilden, Germany) and extracting the RNA using RNeasy® Plus Mini Kit (Qiagen). After determining RNA concentrations by spectrophotometry, 500–800 ng of total RNA was used for cDNA synthesis. Reverse transcription was conducted using the Omniscript RT Kit (Qiagen). Quantitative real-time PCR was performed using the SsoAdvanced Universal SYBR® Green Supermix (Bio-Rad Laboratories, Hercules, CA). The specificity of primers was confirmed by melting curve analysis and gel electrophoresis. All primers were purchased from Integrated DNA Technologies (Table S1).

Influenza A viruses and viral titer quantification

Influenza A/Hong Kong/8/68 (H3N2) and influenza A/WSN/33 (H1N1) viruses were purchased from American Type Culture Collection (ATCC, Manassas, VA) and were propagated following established protocols.[67] Stock viral titers were determined by plaque assays that were performed using an established protocol.[68] In brief, confluent MDCK.2 cell monolayers were cultured in 12-well plates with DMEM supplemented with 10% FBS and 1× Pen-Strep, washed with DPBS and infection medium, inoculated with 0.2 mL of 10-fold serial dilutions of influenza virus samples for 1 h at 37 °C, washed with infection medium, and then overlaid with 1 mL of a mixture of overlay medium and 2% Oxoid™ Purified Agarose (Thermo Fisher) at 1:1 volume ratio supplemented with 2 μg mL^{-1} TPCK-treated trypsin (Sigma Aldrich). 3 days after incubation at 37 °C under 5% CO$_2$, the cells were fixed with 4% paraformaldehyde (PFA, Thermo Fisher) and stained with crystal violet (Sigma Aldrich) to visualize the plaques.

Virus titers were determined as plaque-forming units per milliliter (PFU mL^{-1}).

The human Lung Chip model of influenza infection

Microfluidic two-channel Organ Chip microfluidic devices and the Zoë® Culture Module were purchased from Emulate, Inc. (Boston, MA). Chips were activated using ER1/ER2 reagents (Emulate), washed with DPBS, coated with 150 μg mL^{-1} human collagen IV (Advanced Biomatrix, Carlsbad, CA) and 30 μg mL^{-1} human laminin (Sigma Aldrich), and were then incubated at 37 °C overnight on day 0. On day 1, chips were washed with DPBS, and were seeded with HPMECs (Lonza, Basel, Switzerland) (expanded to passage 5 before used) at the density of 8×10^6 cells per mL in the basal channel, and human primary AECs (Innoprot, Bizkaia, Spain) (obtained at passage 0 and used without expansion) at the density of 1×10^6 cells per mL in the apical channel. Chips were then incubated at 37 °C with 5% CO$_2$ overnight for cell adherence. On day 2, chips were washed with cell culture media and were connect to Pod® (Emulate) (Fig. S7A) placed into the Zoë® Culture Module with AEC culture medium (Innoprot) flowing in the apical channel and EGM®-2MV (Lonza) flowing in the basal channel at 30 μL h^{-1} (Fig. S7B). The Zoë® Culture Module enabled automated flow culture at this stage. The respective medium for each channel was constantly refreshed and the flow was maintained for 3 days. On day 5, ALI was established in the chips by flowing the apical channel at 1000 μL h^{-1} while keeping the flow rate in the basal channel at 0 μL h^{-1} for 5 min, until medium in the apical channel was emptied (Fig. S7C). Chips were thereafter fed through the basal channel by fresh EGM2MV but with 0.5% FBS (termed as "flow media") at 30 μL h^{-1} for 2 days (Fig. S7D). On day 7, mechanical strain was adjusted from 0 to 5% and frequency was adjusted from 0 to 0.25 Hz to mimic the breathing motion-induced mechanical deformation in human alveoli (Fig. S7E). On day 11, chips were ready for infection and/or transfection experiments.

To carry out IAV infections, the chips were disconnected from flow and 35 μL of diluted viral inoculate (MOI = 1) was added to each apical channel to infect the epithelial cells. Chips were kept at static condition at 37 °C under 5% CO$_2$ for 2 h, after which the apical channel was washed with DPBS and emptied to recreate the ALI and the chips were again exposed to basal fluid flow and cyclic breathing motions.

RNA delivery in the human Lung Chip

Human primary AECs cultured in the Lung Chip were transfected with GFP mRNA or Cas13d mRNA plus crRNA using LMM (Thermo Fisher) following the manufacturer's instructions. 3 μL of the reagent was used per 1 μg of mRNA. The mixture was finally diluted to 1 pmol mL^{-1} of Cas13d mRNA concentration using epithelial cell culture medium and perfused through the apical channel at 30 μL h^{-1} overnight (roughly 16 h), after which chips were analyzed or

returned to ALI culture. The flow rate in the basal channel was maintained at 30 μL h^{-1} before, during, and after transfection. To extract the viral RNA, chips were disconnected from flow, placed in a biosafety cabinet, an empty 200 μL filtered tip was inserted to the apical channel outlet, and 100 μl DPBS was injected into the apical channel and retrieved ("apical wash"); the sample was stored at −80 °C until used.

Recruitment of immune cells on-chip

De-identified human patient-derived apheresis collars (by-product of platelet isolation) were obtained from the Crimson Biomaterials Collection Core Facility under approval IRB protocols (#22470); informed written consent was not required. Human PBMCs were isolated by density centrifugation using Lymphoprep (StemCell Technologies, Vancouver, Canada). At 48 h post crRNA treatment, PBMCs were labeled with Cell Tracker Green (10 μM; Thermo Fisher) for 20 min at 37 °C, washed, and re-suspended in flow medium (2 × 10^7 cells per mL). Chips were removed from the Emulate Pod chip holder, and 25 μL of the cell suspension was flushed through the basal vascular channel. The chips were then flipped upside down, and the PBMCs were allowed to adhere under static conditions at 37 °C for 2 h before flipping the chips back. The basal channel was then washed with 100 μL flow medium to wash out unattached cells and the chips were immediately imaged under a fluorescent microscope. Cells were manually counted using Photoshop software (San Jose, CA).

Transcriptomic analysis

For transcriptomic analysis, the apical channel of the Lung Chips was washed with DPBS and then a new empty 200 μL filtered tip was inserted into the channel outlet, and 100 μl Buffer RLT Plus (Qiagen) was injected to fill the channel. The epithelial cells were then lysed by quickly pressing and releasing the micropipette plunger five times, and the lysates were collected and stored at −80 °C until shipped to Azenta Life Sciences (Burlington, MA) for bulk RNA-seq. The paired reads were mapped to the *Homo sapiens* GRCh38 reference genome using the STAR aligner v.2.5.2b, and unique gene hit counts were calculated by using featureCounts from the Subread package v.1.5.2. DEG analysis was performed with the DESeq2 R package1, which tests for differential expression based on a model using the negative binomial distribution. Adjusted *P*-value < 0.01 and fold change > 1.2 or < 0.8 were used to define DEGs. GSEA was using the fgsea R package and the fgseaMultilevel() function 1. KEGG gene set collection from the Molecular Signatures Database (MSigDB)[2,3] was curated using the msigdbr R package.[4] Prior to running GSEA, the list of gene sets was filtered to include only gene sets with between 5 and 1000 genes. RNA-seq data analyses were performed using Pluto software (**https://app.pluto.bio/**). GOBP terms associated with downregulated DEGs were analyzed using Database for Annotation, Visualization and Integrated Discovery (DAVID 2021).[69] All bulk RNA-seq data have been uploaded to the National Center for Biotechnology Information (NCBI) database and made publicly available with the accession number GSE272709.

Immunofluorescence microscopic analysis

For immunofluorescence microscopy studies, chips were rinsed with DPBS and were fixed using 4% PFA for 15 min at room temperature (RT). Chips were then rinsed with DPBS, permeabilized with 0.1% Triton X-100 for 10 min at RT, rinsed with DPBS, and then blocked with 10% goat serum (Thermo Fisher) overnight at 4 °C. The following day, chips were rinsed with DPBS, and were then incubated with primary antibodies with 5% goat serum overnight at 4 °C. The day after, chips were rinsed with DPBS, and incubated with secondary antibodies for 1 h at RT. After twice washing with DPBS, chips were mounted with DAPI (Sigma) and thoroughly rinsed before being imaged on a Zeiss LSM 980 confocal microscopy (Oberkochen, Germany). If using conjugated antibodies, after serum blocking, chips were rinsed and were incubated with the antibodies with 5% goat serum overnight at 4 °C, which were then mounted with DAPI the next day and imaged. All antibody information is listed in Table S2.

Statistical analysis

Data reported in this study are displayed as mean values ± standard deviation (SD). Graphing and statistical comparison were performed using Prism 10.3.1 (GraphPad Software, San Diego, CA). Data were checked for normality and all were found to be normally distributed. Two-group comparisons were assessed using the unpaired *t* test, and comparisons of more than two groups were analyzed by one-way ANOVA with Tukey's multiple comparisons. *P* values less than 0.05 were considered to be statistically significant (*, $P < 0.05$; **, $P < 0.01$; ***, $P < 0.001$; ****, $P < 0.0001$; ns, not significant).

Author contributions

Y. M. and D. E. I. conceptualized the project. H. B. acquired the crRNA design. R. R. P. performed the sequence identity analysis. Y. M., P. D. and D. O. A. performed the transfection efficiency analyses. Y. M., A. J., R. P., J. J. and C. B. performed the experiments and analyses. C. B. performed team management. Y. M. prepared the figures and tables, and wrote the manuscript. N. A. and D. E. I. reviewed and edited the manuscript. All authors approved the final version of the manuscript.

Conflicts of interest

N. A. is a co-founder of BioDevek, Inc., and has financial interests in SpideRx. D. E. I. is a founder, board member, SAB chair, and holds equity in Emulate, Inc. C. B. is a former employee of Emulate, Inc. and holds equity interests in Emulate, Inc.

Data availability

Acknowledgements

References

1 O. O. Abudayyeh, J. S. Gootenberg, P. Essletzbichler, S. Han, J. Joung, J. J. Belanto, V. Verdine, D. B. T. Cox, M. J. Kellner, A. Regev, E. S. Lander, D. F. Voytas, A. Y. Ting and F. Zhang, *Nature*, 2017, **550**, 280–284.

2 C. Xu, Y. Zhou, Q. Xiao, B. He, G. Geng, Z. Wang, B. Cao, X. Dong, W. Bai, Y. Wang, X. Wang, D. Zhou, T. Yuan, X. Huo, J. Lai and H. Yang, *Nat. Methods*, 2021, **18**, 499–506.

3 J. T. Granados-Riverón and G. Aquino-Jarquin, *Cancer Res.*, 2018, **78**, 4107–4113.

4 M. R. O'Connell, *J. Mol. Biol.*, 2019, **431**, 66–87.

5 U. Unniyampurath, R. Pilankatta and M. N. Krishnan, *Int. J. Mol. Sci.*, 2016, **17**, 291.

6 W. X. Yan, S. Chong, H. Zhang, K. S. Makarova, E. V. Koonin, D. R. Cheng and D. A. Scott, *Mol. Cell*, 2018, **70**, 327–339 e325.

7 Y. C. Hsieh, T. Z. Wu, D. P. Liu, P. L. Shao, L. Y. Chang, C. Y. Lu, C. Y. Lee, F. Y. Huang and L. M. Huang, *J. Formosan Med. Assoc.*, 2006, **105**, 1–6.

8 P. Spreeuwenberg, M. Kroneman and J. Paget, *Am. J. Epidemiol.*, 2018, **187**, 2561–2567.

9 J. Paget, P. Spreeuwenberg, V. Charu, R. J. Taylor, A. D. Iuliano, J. Bresee, L. Simonsen, C. Viboud and N. Global Seasonal Influenza-associated Mortality Collaborator and G. L. C. Teams*, *J. Global Health*, 2019, **9**, 020421.

10 Centers for Disease Control and Prevention, 2023, **https://www.cdc.gov/flu-burden/php/about/index.html**.

11 Z. Shriver, J. M. Trevejo and R. Sasisekharan, *Front. Immunol.*, 2015, **6**, 315.

12 S. Duwe, *GMS Infect. Dis.*, 2017, **5**, Doc04.

13 W. Shao, X. Li, M. U. Goraya, S. Wang and J. L. Chen, *Int. J. Mol. Sci.*, 2017, **18**, 1650.

14 C. A. Freije, C. Myhrvold, C. K. Boehm, A. E. Lin, N. L. Welch, A. Carter, H. C. Metsky, C. Y. Luo, O. O. Abudayyeh, J. S. Gootenberg, N. L. Yozwiak, F. Zhang and P. C. Sabeti, *Mol. Cell*, 2019, **76**, 826–837 e811.

15 T. R. Abbott, G. Dhamdhere, Y. Liu, X. Lin, L. Goudy, L. Zeng, A. Chemparathy, S. Chmura, N. S. Heaton, R. Debs, T. Pande, D. Endy, M. F. La Russa, D. B. Lewis and L. S. Qi, *Cell*, 2020, **181**, 865–876 e812.

16 A. Challagulla, K. A. Schat and T. J. Doran, *Methods Protoc.*, 2021, **4**, 40.

17 E. L. Blanchard, D. Vanover, S. S. Bawage, P. M. Tiwari, L. Rotolo, J. Beyersdorf, H. E. Peck, N. C. Bruno, R. Hincapie, F. Michel, J. Murray, H. Sadhwani, B. Vanderheyden, M. G. Finn, M. A. Brinton, E. R. Lafontaine, R. J. Hogan, C. Zurla and P. J. Santangelo, *Nat. Biotechnol.*, 2021, **39**, 717–726.

18 L. C. Chaves, N. Orr-Burks, D. Vanover, V. V. Mosur, S. R. Hosking, E. K. P. Kumar, H. Jeong, Y. Jung, J. A. Assumpção and H. E. Peck, *PLoS Pathog.*, 2024, **20**, e1012345.

19 X. Lin, Y. Liu, A. Chemparathy, T. Pande, M. La Russa and L. S. Qi, *Cell Rep. Med.*, 2021, **2**, 100245.

20 H.-H. Wessels, A. Méndez-Mancilla, X. Guo, M. Legut, Z. Daniloski and N. E. Sanjana, *Nat. Biotechnol.*, 2020, **38**, 722–727.

21 D. Huh, B. D. Matthews, A. Mammoto, M. Montoya-Zavala, H. Y. Hsin and D. E. Ingber, *Science*, 2010, **328**, 1662–1668.

22 D. E. Ingber, *Nat. Rev. Genet.*, 2022, **23**, 467–491.

23 L. Si, H. Bai, M. Rodas, W. Cao, C. Y. Oh, A. Jiang, R. Moller, D. Hoagland, K. Oishi, S. Horiuchi, S. Uhl, D. Blanco-Melo, R. A. Albrecht, W. C. Liu, T. Jordan, B. E. Nilsson-Payant, I. Golynker, J. Frere, J. Logue, R. Haupt, M. McGrath, S. Weston, T. Zhang, R. Plebani, M. Soong, A. Nurani, S. M. Kim, D. Y. Zhu, K. H. Benam, G. Goyal, S. E. Gilpin, R. Prantil-Baun, S. P. Gygi, R. K. Powers, K. E. Carlson, M. Frieman, B. R. tenOever and D. E. Ingber, *Nat. Biomed. Eng.*, 2021, **5**, 815–829.

24 H. Bai, L. Si, A. Jiang, C. Belgur, Y. Zhai, R. Plebani, C. Y. Oh, M. Rodas, A. Patil, A. Nurani, S. E. Gilpin, R. K. Powers, G. Goyal, R. Prantil-Baun and D. E. Ingber, *Nat. Commun.*, 2022, **13**, 1928.

25 Y. Man, Y. Zhai, A. Jiang, H. Bai, A. Gulati, R. Plebani, R. J. Mannix, G. E. Merry, G. Goyal and C. Belgur, bioRxiv, 2024, preprint, DOI: **10.1101/2024.1108.1113.607799**.

26 L. Zeng, Y. Liu, X. H. Nguyenla, T. R. Abbott, M. Han, Y. Zhu, A. Chemparathy, X. Lin, X. Chen, H. Wang, D. A. Rane, J. M. Spatz, S. Jain, A. Rustagi, B. Pinsky, A. E. Zepeda, A. P. Kadina, J. A. Walker, K. Holden, N. Temperton, J. R. Cochran, A. E. Barron, M. D. Connolly, C. A. Blish, D. B. Lewis, S. A. Stanley, M. F. La Russa and L. S. Qi, *Nat. Commun.*, 2022, **13**, 2766.

27 H. Yin, C. Q. Song, S. Suresh, Q. Wu, S. Walsh, L. H. Rhym, E. Mintzer, M. F. Bolukbasi, L. J. Zhu, K. Kauffman, H. Mou, A. Oberholzer, J. Ding, S. Y. Kwan, R. L. Bogorad, T. Zatsepin, V. Koteliansky, S. A. Wolfe, W. Xue, R. Langer and D. G. Anderson, *Nat. Biotechnol.*, 2017, **35**, 1179–1187.

28 D. Chen, K. T. Love, Y. Chen, A. A. Eltoukhy, C. Kastrup, G. Sahay, A. Jeon, Y. Dong, K. A. Whitehead and D. G. Anderson, *J. Am. Chem. Soc.*, 2012, **134**, 6948–6951.

29 S. J. Shepherd, C. C. Warzecha, R. Yadavali, R. El-Mayta, M. G. Alameh, L. Wang, D. Weissman, J. M. Wilson, D. Issadore and M. J. Mitchell, *Nano Lett.*, 2021, **21**, 5671–5680.

30 N. Segovia, P. Dosta, A. Cascante, V. Ramos and S. Borros, *Acta Biomater.*, 2014, **10**, 2147–2158.

31 P. Dosta, N. Segovia, A. Cascante, V. Ramos and S. J. A. B. Borrós, *Acta Biomater.*, 2015, **20**, 82–93.

32 P. Dosta, V. Ramos and S. Borrós, *Mol. Syst. Des. Eng.*, 2018, **3**, 677–689.

33 A. Iwasaki and P. S. Pillai, *Nat. Rev. Immunol.*, 2014, **14**, 315–328.

34 Y. Ai, D. Liang and J. E. Wilusz, *Nucleic Acids Res.*, 2022, **50**, e65.

35 J. F. Bot, J. van der Oost and N. Geijsen, *Curr. Opin. Biotechnol.*, 2022, **78**, 102789.

36 H. Matsui, L. G. Johnson, S. H. Randell and R. C. Boucher, *J. Biol. Chem.*, 1997, **272**, 1117–1126.

37 C. M. Bartman, K. E. Stelzig, D. R. Linden, Y. S. Prakash and S. E. Chiarella, *Am. J. Physiol.*, 2021, **321**, L280–L286.

38 J. Kim, A. Jozic, Y. Lin, Y. Eygeris, E. Bloom, X. Tan, C. Acosta, K. D. MacDonald, K. D. Welsher and G. Sahay, *ACS Nano*, 2022, **16**, 14792–14806.

39 X. Hou, T. Zaks, R. Langer and Y. Dong, *Nat. Rev. Mater.*, 2021, **6**, 1078–1094.

40 X. Han, H. Zhang, K. Butowska, K. L. Swingle, M. G. Alameh, D. Weissman and M. J. Mitchell, *Nat. Commun.*, 2021, **12**, 7233.

41 Y. Dong, K. T. Love, J. R. Dorkin, S. Sirirungruang, Y. Zhang, D. Chen, R. L. Bogorad, H. Yin, Y. Chen, A. J. Vegas, C. A. Alabi, G. Sahay, K. T. Olejnik, W. Wang, A. Schroeder, A. K. Lytton-Jean, D. J. Siegwart, A. Akinc, C. Barnes, S. A. Barros, M. Carioto, K. Fitzgerald, J. Hettinger, V. Kumar, T. I. Novobrantseva, J. Qin, W. Querbes, V. Koteliansky, R. Langer and D. G. Anderson, *Proc. Natl. Acad. Sci. U. S. A.*, 2014, **111**, 3955–3960.

42 J. Hur, I. Park, K. M. Lim, J. Doh, S.-G. Cho and A. J. Chung, *ACS Nano*, 2020, **14**, 15094–15106.

43 Q. Zhao, M. Liang and Y. Ai, *Sens. Actuators, B*, 2025, 137953.

44 C. Kwon and A. J. Chung, *Lab Chip*, 2023, **23**, 1758–1767.

45 A. Stejskalova, K. Calderon, D. B. Chou, A. Gulati, J. F. Feitor, Z. Izadifar, O. Gutzeit, Y. Bouchibti, S. Chen, R. Plebani, J. Cotton, J. Hughes, T. Ferrante, B. Budnik, G. Goyal, A. Junaid, C. B. Lebrilla and D. E. Ingber, *bioRxiv*, 2025, preprint, DOI: **10.1101/2025.05.01.651107**.

46 Z. Izadifar, J. Cotton, S. Chen, V. Horvath, A. Stejskalova, A. Gulati, N. T. LoGrande, B. Budnik, S. Shahriar and E. R. Doherty, *Nat. Commun.*, 2024, **15**, 4578.

47 O. Andries, S. Mc Cafferty, S. C. De Smedt, R. Weiss, N. N. Sanders and T. Kitada, *J. Controlled Release*, 2015, **217**, 337–344.

48 K. H. Loomis, K. E. Lindsay, C. Zurla, S. M. Bhosle, D. A. Vanover, E. L. Blanchard, J. L. Kirschman, R. V. Bellamkonda and P. J. Santangelo, *Bioconjugate Chem.*, 2018, **29**, 3072–3083.

49 P. M. Tiwari, D. Vanover, K. E. Lindsay, S. S. Bawage, J. L. Kirschman, S. Bhosle, A. W. Lifland, C. Zurla and P. J. Santangelo, *Nat. Commun.*, 2018, **9**, 3999.

50 Y. V. Svitkin, Y. M. Cheng, T. Chakraborty, V. Presnyak, M. John and N. Sonenberg, *Nucleic Acids Res.*, 2017, **45**, 6023–6036.

51 P. Wang, M. S. Nair, L. Liu, S. Iketani, Y. Luo, Y. Guo, M. Wang, J. Yu, B. Zhang, P. D. Kwong, B. S. Graham, J. R. Mascola, J. Y. Chang, M. T. Yin, M. Sobieszczyk, C. A. Kyratsous, L. Shapiro, Z. Sheng, Y. Huang and D. D. Ho, *Nature*, 2021, **593**, 130–135.

52 W. F. Garcia-Beltran, E. C. Lam, K. St Denis, A. D. Nitido, Z. H. Garcia, B. M. Hauser, J. Feldman, M. N. Pavlovic, D. J. Gregory, M. C. Poznansky, A. Sigal, A. G. Schmidt, A. J. Iafrate, V. Naranbhai and A. B. Balazs, *Cell*, 2021, **184**, 2523.

53 H. J. E. Baddeley and M. Isalan, *Front. Genome Ed.*, 2021, **3**, 745559.

54 R. Alonso-Roman, A. S. Mosig, M. T. Figge, K. Papenfort, C. Eggeling, F. H. Schacher, B. Hube and M. S. Gresnigt, *Nat. Microbiol.*, 2024, **9**, 891–904.

55 V. Ektnitphong, B. R. Dias, P. C. Campos and M. U. Shiloh, *Dis. Models Mech.*, 2025, dmm. 052085.

56 C. Richter, L. Latta, D. Harig, P. Carius, J. D. Stucki, N. Hobi, A. Hugi, P. Schumacher, T. Krebs and A. Gamrekeli, *Bioeng. Transl. Med.*, 2025, **10**, e10715.

57 C. H. Luk, G. L. Conway, K. J. Goh, A. Fearns, I. Rodriguez-Hernandez, N. J. Day, N. Athanasiadi, R. D'Antuono, E. Pellegrino, J. D. Stucki, N. Hobi and M. G. Gutierrez, *bioRxiv*, 2025, preprint, DOI: **10.1101/2025.03.14.643230**.

58 L. Si, H. Bai, C. Y. Oh, L. Jin, R. Prantil-Baun and D. E. Ingber, *Microbiol. Spectrum*, 2021, **9**, e0025721.

59 U. Marx, T. Akabane, T. B. Andersson, E. Baker, M. Beilmann, S. Beken, S. Brendler-Schwaab, M. Cirit, R. David, E. M. Dehne, I. Durieux, L. Ewart, S. C. Fitzpatrick, O. Frey, F. Fuchs, L. G. Griffith, G. A. Hamilton, T. Hartung, J. Hoeng, H. Hogberg, D. J. Hughes, D. E. Ingber, A. Iskandar, T. Kanamori, H. Kojima, J. Kuehnl, M. Leist, B. Li, P. Loskill, D. L. Mendrick, T. Neumann, G. Pallocca, I. Rusyn, L. Smirnova, T. Steger-Hartmann, D. A. Tagle, A. Tonevitsky, S. Tsyb, M. Trapecar, B. Van de Water, J. Van den Eijnden-van Raaij, P. Vulto, K. Watanabe, A. Wolf, X. Zhou and A. Roth, *ALTEX*, 2020, **37**, 365–394.

60 US Congress, 2022, **https://www.congress.gov/bill/117th-congress/senate-bill/5002**.

61 Q. Ge, M. T. McManus, T. Nguyen, C. H. Shen, P. A. Sharp, H. N. Eisen and J. Chen, *Proc. Natl. Acad. Sci. U. S. A.*, 2003, **100**, 2718–2723.

62 S. L. Williams, L. Qi, Z. M. Sheng, Y. Xiao, A. Freeman, L. Matthews, S. F. Legaspi, E. Fodor and J. K. Taubenberger, *Sci. Adv.*, 2024, **10**, eads5735.

63 E. Robinson, K. D. MacDonald, K. Slaughter, M. McKinney, S. Patel, C. Sun and G. Sahay, *Mol. Ther.*, 2018, **26**, 2034–2046.

64 Y. Man, D. Maji, R. An, S. P. Ahuja, J. A. Little, M. A. Suster, P. Mohseni and U. A. Gurkan, *Lab Chip*, 2021, **21**, 1036–1048.

65 Y. Man, D. H. Wu, R. An, P. Wei, K. Monchamp, U. Goreke, Z. Sekyonda, W. J. Wulftange, C. Federici and A. Bode, *Sens. Diagn.*, 2023, **2**, 457–467.

66 Y. Man, E. Kucukal, R. An, Q. D. Watson, J. Bosch, P. A. Zimmerman, J. A. Little and U. A. Gurkan, *Lab Chip*, 2020, **20**, 2086–2099.

67 A. L. Balish, J. M. Katz and A. I. Klimov, *Curr. Protoc. Microbiol.*, 2013, **29**, 15G.1.1–15G.1.24.

68 I. E. Galani, V. Triantafyllia, E. E. Eleminiadou and E. Andreakos, *STAR Protoc.*, 2022, **3**, 101151.

69 D. W. Huang, B. T. Sherman and R. A. Lempicki, *Nat. Protoc.*, 2009, **4**, 44–57.